RSC Advances

PAPER

View Article Online
View Journal | View Issue

Cite this: *RSC Adv.*, 2024, **14**, 13837

Elucidating the performance of hexamethylene tetra-amine interlinked bimetallic NiCo-MOF for efficient electrochemical hydrogen and oxygen evolution

Rida Zahid,[a] Muhammad Ramzan Abdul Karim, *[b] Fahd Sikandar Khan[a] and Mohsin Ali Marwat[b]

Bimetallic metal–organic frameworks (MOFs) play a significant role in the electrocatalysis of water due to their large surface area and availability of increased numbers of pores. For the inaugural time, we examine the effectiveness of a hexamethylene tetra-amine (HMT)-induced 3D NiCo-MOF-based nanostructure as a potent bifunctional electrocatalyst with superior performance for overall water splitting in alkaline environments. The structural, morphological, and electrochemical properties of the as-synthesized bifunctional catalyst were examined thoroughly before analyzing its behavior towards electrochemical water splitting. The HMT-based NiCo-MOF demonstrated small overpotential values of 274 mV and 330 mV in reaching a maximum current density of 30 mA cm^{-2} for hydrogen and oxygen evolution mechanisms, respectively. The Tafel parameter also showed favorable HER/OER reaction kinetics, with slopes of 78 mV dec^{-1} and 86 mV dec^{-1} determined during the electrochemical evaluation. Remarkably, the NiCo-HMT electrode exhibited a double-layer capacitance of 4 mF cm^{-2} for hydrogen evolution and 23 mF cm^{-2} for oxygen evolution, while maintaining remarkable stability even after continuous operation for 20 hours. This research offers a valuable blueprint for implementing a cost-effective and durable MOF-based bifunctional catalytic system that has proven to be effective for complete water splitting. Decomposition of water under higher current densities is crucial for effective long-term generation and commercial consumption of hydrogen.

Received 13th January 2024
Accepted 5th April 2024

DOI: 10.1039/d4ra00340c

rsc.li/rsc-advances

1. Introduction

Increasing degradation of the environment, mounting energy-related issues, and depletion of fossil fuel reserves are compelling researchers worldwide to investigate contemporary and sustainable energy reservoirs, transportation, and other methodologies.[1–4] Hydrogen, with its impressive hydrometric density of 142 MJ kg^{-1} and a wide array of manufacturing sources is emerging as a favorable, environmentally friendly energy carrier that is poised to be a substitute for fossil fuels.[5,6] Among various production methods, electrochemical water splitting stands out as the most efficient and environmentally sustainable approach for generating pure and eco-friendly hydrogen. This method is particularly advantageous due to the profusion of water sources and their green emissions.[7,8] The H_2 evolution reaction (HER), in addition to the O_2 evolution reaction (OER), has great importance as a crucial electrochemical process in fuel cells.[9–11] The HER is a common reaction that occurs when water splits *via* a two-step transfer kinetics mechanism.[12] In contrast to the HER, which requires just two electrons, the OER requires four proton–electron transfers, which results in a greater overpotential throughout the entire water-splitting system. This results in the OER having slower kinetics and being more complex.[13] Therefore, it is imperative to develop the electrocatalysts that demonstrate significantly improved performance and stability to facilitate the efficient reaction mechanisms.[14,15] Transition metals, such as platinum (Pt), iridium (Ir), and ruthenium (Ru), play a pivotal role in significantly enhancing electrocatalytic efficiency, and this has led to widespread adoption of these electrode materials and on a large scale.[16] Nevertheless, their high cost and limited availability serve as obstacles that hinder their expanded use for water splitting.[17] Given these factors, there is a growing need to continue to explore alternative, non-precious metal electrocatalysts that are more accessible, more cost-effective, and offer high activity and high stability. These substitutes aim to replicate or even surpass the catalytic performance of noble metals.[18]

[a]*Faculty of Engineering Sciences, Ghulam Ishaq Khan Institute of Engineering Sciences and Technology, Topi, 23640, Pakhtunkhwa, Pakistan*

[b]*Faculty of Materials and Chemical Engineering, Ghulam Ishaq Khan Institute of Engineering Sciences and Technology, Topi, 23640, Khyber Pakhtunkhwa, Pakistan. E-mail: ramzan.karim@giki.edu.pk; ramzan1109@hotmail.com; Tel: +92 (0938) 281026*

Numerous efforts have been focused on the advancement of electrocatalysts by employing transition metal sulfides, phosphides, and dichalcogenides.[18,19] The majority of these electrocatalysts typically demonstrate singular performance in either the HER, OER, or MOR (methanol oxidation reaction). Metal–organic frameworks (MOFs), a category of hybrid porous nanomaterials that fuse organic and inorganic components, feature inorganic secondary building units (comprising metal cores or clusters) connected to organic bridging linkers through coordination bonds. These intriguing structures have captured increasing attention from researchers and have been investigated across diverse domains, including gas separation, photo/electrocatalysis, absorption, advanced medical therapies, sensor technology, and energy storage.[20–23] Their distinctive attributes, including high surface area, porosity, adjustable pore configurations, and chemical modifiability, contribute to their broad utility.[24–27] Electrocatalysts rooted in MOFs, and those derived from MOFs, have undergone extensive development in a range of applications, including overall water decomposition,[28] zinc–air batteries,[29] CO oxidation, CO_2 reduction,[30] and the MOR.[31] Selection of organic linkers plays a significant part in shaping the characteristics of the MOFs. Hexamethyl tetraamine (HMT), an organic ligand, has been widely used in the preparation of MOFs.[32] Its intrinsic rigidity and versatile coordination geometries make it well suited for constructing MOFs with distinct properties. In many cases, pristine MOFs, when employed as electrocatalysts, cannot demonstrate ideal behavior towards electrochemical systems.[33] By introducing two metal ions during synthesis of the framework, the resulting bimetallic MOFs are capable of surpassing the performance of monometallic MOFs in certain fields.[34] The presence of bimetals not only widens the active available area but also enhances the overall productivity of electrochemical cells.[35]

Among the transition metals, nickel (Ni), as an earth-abundant element, stands out owing to its remarkable electrical conductivity, corrosion resistance, electrocatalytic performance, and ductility. These properties make it highly effective and versatile for use in various fields, including supercapacitors, batteries, and electrocatalysts.[36] Ni-based oxides, mixed-metal oxides, hydroxides, and nickel-based metal–organic frameworks are commonly used in the process of electrocatalysis.[37,38] In bimetallic frameworks, the presence of two metals with varied valence, vacant coordination sites, and atomic imperfections contributes to the creation of active sites, which in turn leads to a reduced overpotential. This characteristic is especially advantageous, particularly in the context of the OER mechanism.[39] In 2020, Cui *et al.* synthesized bimetallic $NiCo(HAB)_2$ with a Ni : Co ratio of 3 : 1. The electrocatalytic performance of the resulting catalysts in the $Co_xNi_{3-x}(HAB)_2$ MOF, arising from the synergistic interaction between various metal atoms, outperformed that of catalysts derived from individual metal-based MOFs.[40] Electrochemical measurements revealed that within the $Co_xNi_{3-x}(HAB)_2$ MOF with a Co : Ni mass ratio of 1 : 3, notably low overpotentials were observed. These values were 119 mV for the HER and 1.35 V for the OER, at a current density of 10 mA cm^{-1}. In 2020, Yang *et al.* reported the development of dual metal-based electrocatalysts, specifically CoFe-MOF and CoNi-MOF, as well as single metal-based catalysts, such as Co-MOF, for the OER. Among the prepared catalysts, it was observed that CoFe-MOF exhibited superior OER activity compared to Co-MOF and CoNi-MOF. The approach of preparing monometallic and bimetallic electrocatalysts for the HER/OER mechanism not only aids in the exploration of structure–performance relationships at atomic and/or molecular levels but also enables a deeper understanding of interrelated catalytic mechanisms.[41]

Herein, our primary objective was to design a bimetallic NiCo-HMT MOF by integrating metal centers within the HMT linker. Initially, we fabricated the MOF using a hydrothermal approach. The morphological and structural properties of the synthesized material were examined using physical characterization techniques, including X-ray diffraction, Raman spectroscopy, FTIR spectroscopy, scanning electron microscopy, and energy-dispersive X-ray spectroscopy (EDX). To investigate inherent electrochemical properties, we constructed a three-electrode setup. The prepared electrocatalyst demonstrated remarkable performance in the context of overall water catalysis. Furthermore, the extracted Tafel slopes and double-layer capacitance values offer additional insights into the electrochemical behavior of the developed catalysts towards the HER and OER.

2. Experimental methodology

2.1 Materials required

The chemicals required in the formation of the bimetallic MOF, such as nickel(II) chloride ($NiCl_2 \cdot 2H_2O$, ≥99.99%), cobalt(II) chloride ($CoCl_2 \cdot 2H_2O$, ≥99.99%), and organic ligand HMT (≥98.5%), were bought from Sigma-Aldrich. All above-mentioned precursors were of prime quality with 99.9% trace metal basis (≤15.0 ppm trace metal analysis) and could be utilized without further purification.

2.2 Synthesis of NiCo-HMT MOF

The bimetallic NiCo-MOF was prepared using the hydrothermal approach according to procedures already reported in the literature for the production of copper–cobalt-based MOFs.[37] The schematic design of the synthesis is illustrated in Fig. 1. Nickel(II) chloride ($NiCl_2 \cdot 2H_2O$, 2.37 g) and cobalt(II) chloride ($CoCl_2 \cdot 2H_2O$, 2.37 g) were separately dissolved in 25 mL of dimethylformamide (DMF). The beaker was then placed onto a magnetic stirrer containing a 50 mL mixture of both solutions. The HMT linker (0.7 g) was poured into 20 mL of DMF and poured dropwise into the prepared solution, which remained under continuous stirring for 40 minutes. Subsequently, the as-prepared solution was emptied into a Teflon-lined autoclave and kept inside an electric oven at 135 °C for 24 h, after which it was left to cool under ambient temperature. The solution containing the nanoparticles that settled at the bottom of the autoclave reactor was purified with deionized water, methanol, ethanol and acetone, sequentially. The resultant bulk MOF was achieved by drying the powder at 70 °C for 12 hours.

2.3 Fabrication of electrodes

Nickel foam (NF) was employed as a current collector and underwent a purification process by subjecting it to a 3 M HCl

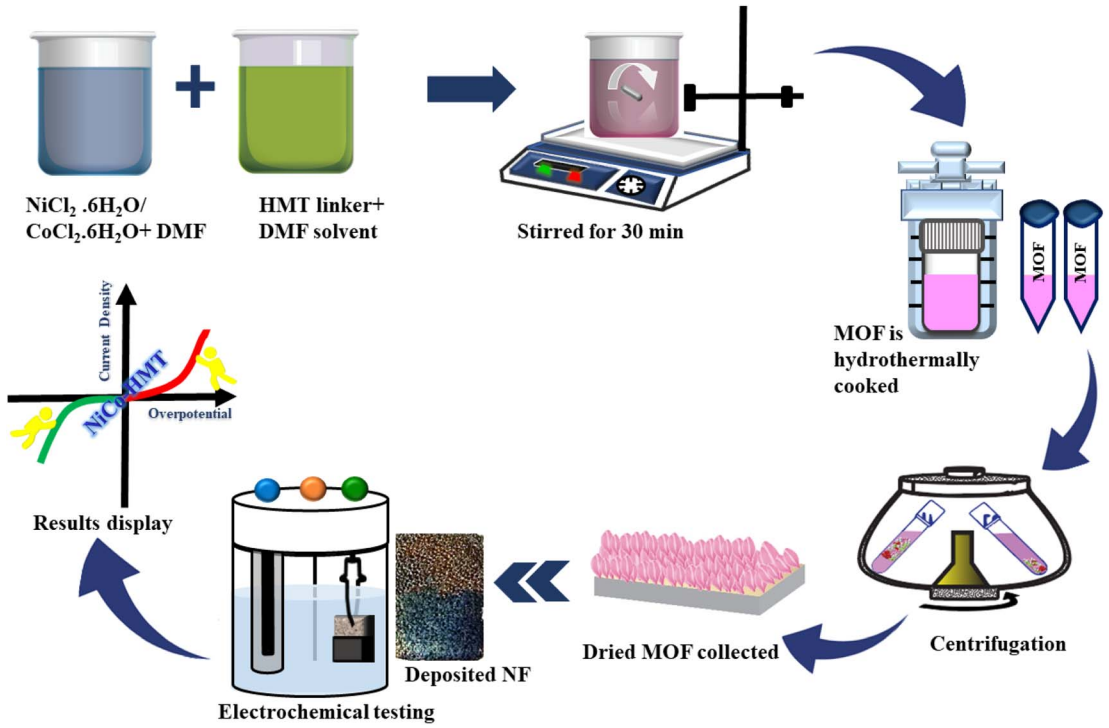

Fig. 1 Schematic illustration of hydrothermal technique employed to synthesize NiCo-HMT MOF.

solution, to eliminate impurities from the surface. The NF was cleansed with acetone and ethanol to ensure its purity, before being dried in a vacuum oven. To prepare a slurry of the as-prepared active material (NiCo-HMT), a mixture was created by combining acetylene black (10 wt%), NMP-PVDF binder (10 wt%), and 80% of the active powdered MOF. The slurry was stirred for 8 hours until a uniform suspension was obtained, which was subsequently drop-cast onto the ~1 × 1 cm^2 NF surface and then left to dry at 70 °C for 4 h.

2.4 Physical characterization

In order to validate the crystallinity and phase integrity of synthesized sample, X-ray diffraction analysis (employing a Bruker diffractometer with graphite-monochromatic Mo-Kα radiation) has been performed. To examine the morphology, elemental composition, and atomic/molecular size of the materials a Nova Nano-SEM microscope operating at 15.0 kV was used, which captured scanning electron microscopy (SEM) images energy dispersive X-ray (EDX) spectroscopy, and generated elemental mapping descriptions. Furthermore, Fourier-transform infrared (FTIR) spectroscopy of generated structures was performed over a frequency range of 650–4000 cm^{-1}. Raman spectroscopic analysis was carried out to verify the expected material formed.

2.5 Electrochemical measurements

The electrochemical activities of manufactured electrode materials towards energy conversion (water splitting, *i.e.* HER/OER) were evaluated in an electrochemical cell with a three-electrode assembly in 1 molar KOH medium. An active sample was utilized as the working electrode, while Hg/HgO and Pt-wire were employed as reference and counter electrodes, respectively. By functionalizing a three-electrode system to investigate the linear sweep voltammetry (LSV) and EIS of both materials, it is possible to obtain a comprehensive understanding of their electrochemical behavior. In addition, LSV analysis was executed to assess the electrochemical response of the material towards water splitting at a constant potential sweep rate of 5 mA cm^{-2}. The HER behavior of all the required samples was evaluated using polarization curves with potential ranging from −0.8 V to −1.5 V, and from 0.1 to 0.9 V for the OER mechanism. In this analysis, all voltages were converted into potential *vs.* reversible hydrogen electrode (RHE) by applying the Nernst equation.

$$E_{RHE} = E_{Hg/HgO} + E_o + 0.059 \times pH$$

Chronoamperometric analysis was conducted to assess the stability and prolonged performance of the as-synthesized catalyst. Furthermore, electrochemical impedance spectroscopy (EIS) measurements were conducted at 5 mV (alternating voltage amplitude) with a frequency limit of 0.1 Hz–100 kHz, to examine the electrical behavior of the as-prepared electrode. In the chronoamperometry experiment, a potential of −0.376 V *vs.* RHE was maintained for a duration of 20 hours for the durability test. To calculate the electrochemical active surface area (ECSA) experimentally, cyclic voltammetry (CV) scans were conducted at scan rates ranging from 20 to 160 mV s^{-1}, to measure the double-layer capacitance (C_{dl}) of the electrocatalyst. The C_{dl} was derived by calculating the linear slopes of Δj ($j_a - j_c$) at 0.05 V *vs.* RHE plotted against scan rates.

3. Results and discussion

3.1 Structural analysis

3.1.1 XRD, FTIR, Raman, SEM and EDX. The appropriate NiCo-HMT powdered sample was chosen for data collection, which was conducted at a temperature of 296 K. To achieve more comprehensive understanding of the crystalline/powdered structure of the designed MOF, XRD analysis was also carried out. Fig. 2(a) demonstrates that the main intensity peaks are visible at 14.18°, 31.2°, 44.8°, 55.8°, 65.2°, and 75.1° for the NiCo-MOF, which correspond to those previously stated in the literature.[42] The peaks at 31.2°, 44.8°, 55.8°, and 65.2° can be indexed to (220), (400), (422) and (440) planes (JCPDS card no. 73-1702).[43] The broader peak at 14.18° indicates the presence of some impurities or lattice defects, while the precision of peaks is linked to the consistency of the crystal lattice and purity level of the sample.[44,45]

The FTIR spectroscopy of the developed nanostructures has been performed in the frequency range 650–4000 cm^{-1} as shown in Fig. 2(b). The NiCo-HMT demonstrates the prominent

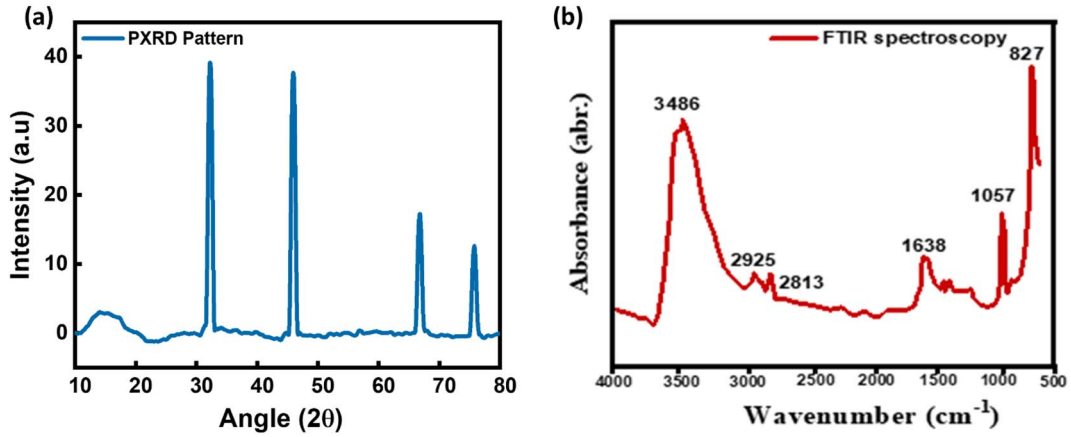

Fig. 2 (a) XRD pattern of the as-prepared bimetallic MOF electrocatalyst. (b) FTIR spectrum of the bimetallic MOF electrocatalyst.

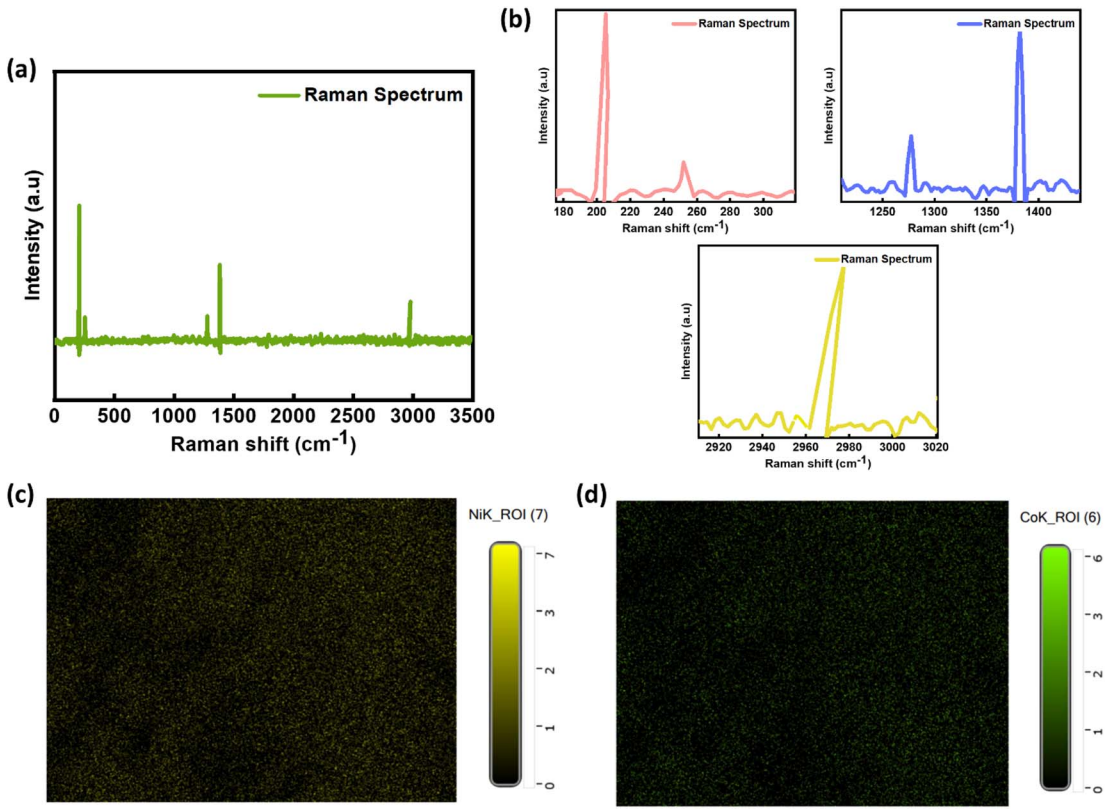

Fig. 3 (a) Raman spectroscopic analysis. (b) Zoomed-in images of Raman spectroscopy. (c) SEM area mapping of nickel in HMT linked NiCo-MOF. (d) SEM area mapping of cobalt in the synthesized HMT linked NiCo-MOF.

peaks at 827 cm^{-1}, 1057 cm^{-1}, 1638 cm^{-1}, 2813 cm^{-1}, 2925 cm^{-1}, and 3486 cm^{-1}. Here in the FTIR spectrum, the peak in high frequency region 3486 cm^{-1} indicates the deeper absorption of the NiCo framework and stretching frequency of hydroxyl (OH) bonding groups from the H_2O molecule.[46] The another peak at 1638 cm^{-1} also indicates the broad OH bond stretching phenomenon. The intensity peak at 1057 cm^{-1} shows the band for composite and hybridized MOFs which may be linked to the vibrational extension of C–H bonded groups.[47] However, M–O and M–O–M bond movements are are represented by intensity peak 660 cm^{-1} (M = Ni and Co).[48] In addition, the peak at 2813 cm^{-1} signifies the C–H bond stretching in aliphatic hydrocarbons, and the peak at 2925 cm^{-1} is associated with C–H bond stretching in methylene and methyl groups.[49]

Raman spectroscopy was performed over the range 50 to 3500 cm^{-1} to analyze chemical bonds and phonon vibrational modes present within the framework. Fig. 3(a and b) shows the Raman spectra of the NiCo-MOF with some of the major peaks. The peaks at very low frequency, such as 204 cm^{-1} and 258 cm^{-1}, indicating the J_2 and A_g vibrational modes of the HMT-based NiCo-MOF.[50,51] The observed peak shift at 1277 cm^{-1} corresponds to the vibrational mode involving C–H bending and out-of-plane bending of the benzene ring.[52] The one major peak at 1380 cm^{-1} is due to D band which is attributed to carbon defects[53,54] while the peak at 2790 cm^{-1} appears due to the 2D band, offering a distinct indication of the presence of the graphitized pi-electron state within the crystal structure.[55]

Morphological and topological scrutiny of the NiCo-MOF was performed using scanning electron microscopy. Fig. 3(c and d) shows the elemental mapping of nickel and cobalt in the NiCo-MOF, while Fig. 4(a and b) shows SEM micrographs of the as-prepared NiCo-MOF at different magnifications. The sample NiCo-MOF exhibited highly porous and distinct flake-like structures (some were spherical) in accord with previously reported data.[56,57] The hollow porous geometry not only offered a greater amount of open space and abundant surface reaction sites, to reduce the diffusion length of electrons and ions but also mitigated structural variations that occurred during electrochemical reactions, leading to remarkable electrochemical behavior. The desired sample exhibited proper volumetric dimensions, which confirmed the 3D morphology of the MOF. Subsequently, EDX measurement was conducted to validate accurate fabrication of the prepared material. Energy-dispersive analysis of the MOF shows prominent peaks corresponding to Ni and Co metals, as well as peaks for carbon (C) and oxygen (O). These findings suggest the presence of organic linkers within the MOF structure and are shown in Fig. 4(c).

3.2 Electrochemical analysis

3.2.1 LSV and Tafel measurements. The electrochemical performance of the prepared electrodes, including bare nickel foam (NF) and NiCo-MOF, was tested in a three-electrode setup, as depicted in Fig. 5. The behavior of all the required samples towards the HER was analyzed by performing linear-sweep

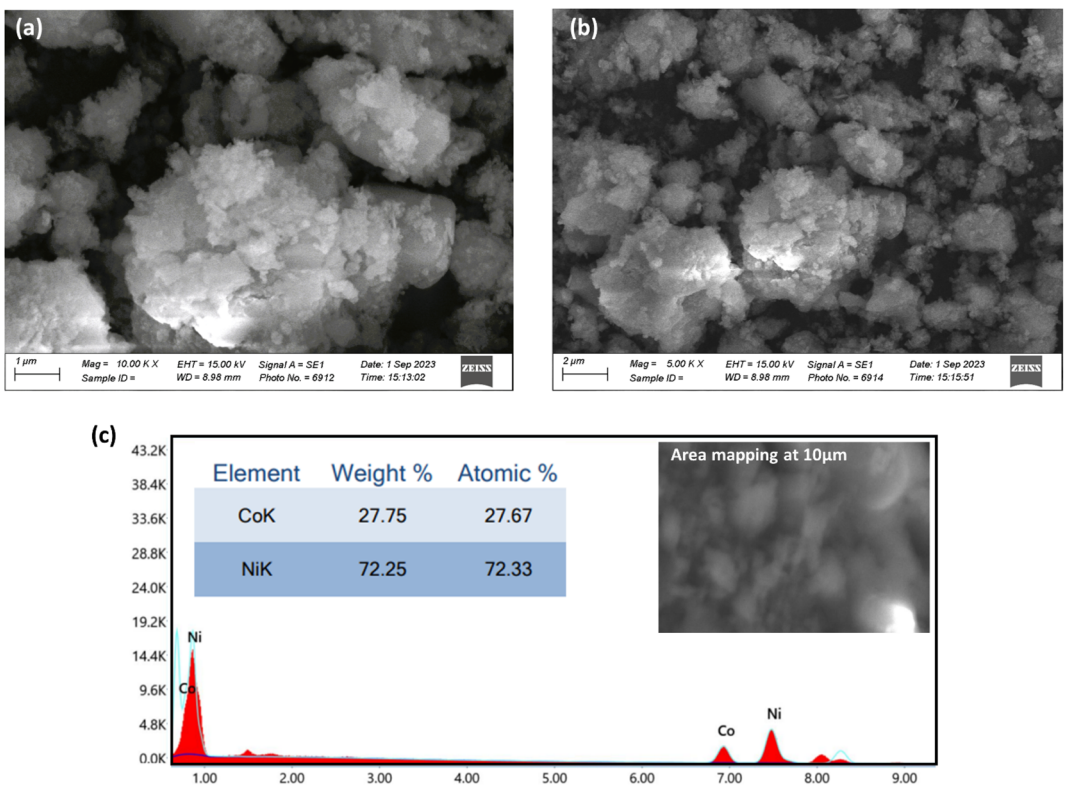

Fig. 4 (a) SEM image at 10000×. (b) Scanning electron micrograph of NiCo framework at 5000×. (c) EDX analysis along with SEM image at 10000× magnification.

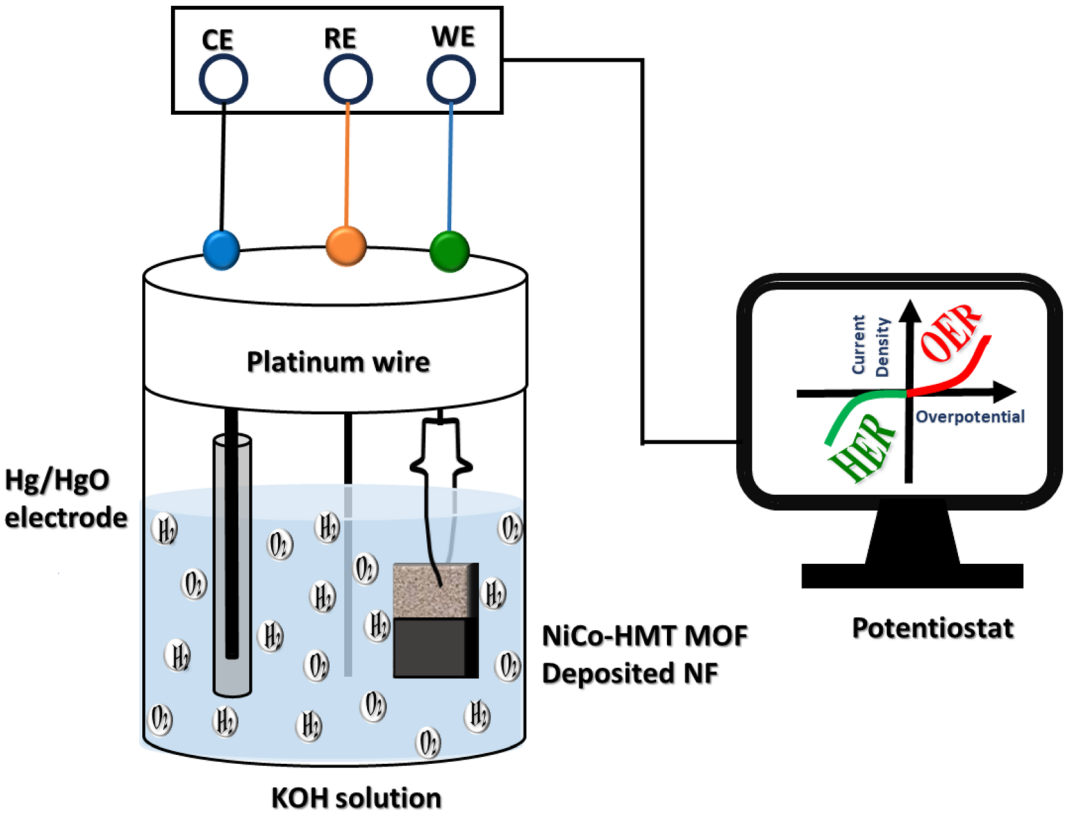

Fig. 5 Three-electrodes setup for catalysis of water.

voltammetry tests in aqueous medium (1 M KOH) with a scanning potential of 5 mV s^{-1}. A plot comparing the LSV performance of both the electrodes is shown in Fig. 6(a). The overpotential (η_{30}) and onset potential (η_0), defined as the voltage required to attain specific current densities of 1 and 30 mA cm^{-2}, were measured to evaluate the electrocatalytic characteristics of the as-prepared catalysts. The overpotential of the electrodes can be measured with respect to the RHE using the Nernst equation and is a necessary parameter to overcome the energy barrier and facilitate chemical reaction. In the LSV plot with *IR* compensation for the HER mechanism, all the samples revealed distinct overpotential values to yield a current density of 30 mA cm^{-2}. The as-prepared bimetallic NiCo-HMT MOF/NF required an overpotential of 274 mV at a scanning potential of 5 mV s^{-1}. The bare NF tested for hydrogen evolution demonstrated an overpotential of 495 mV, which is considerably higher compared to the active material. The NiCo-MOF sample delivered a considerably reduced η_{30} value compared with the bare substrate, suggesting better performance towards hydrogen evolution. Furthermore, the synthesized MOF displayed a very small overpotential value of 337 mV to reach higher current density of 50 mA cm^{-2}, while the bare NF showed a very low current of ~40 mA cm^{-2}. Thus, it is shown that the overpotential values increase linearly at higher current densities. This shows that the NiCo-HMT MOF is a better electrocatalyst, since it exhibits a lower overpotential, indicating more favorable kinetics for the HER. Furthermore, the faster kinetics and efficiency of the electrocatalysts can be analyzed by determining their Tafel slope values from polarization curves, using the following equation.

$$\eta = a + b \log j$$

where b represents the slope value and j is the current density. The Tafel slope for the NiCo-MOF is 78 mV dec^{-1}, which is markedly superior to that of the bare NF catalyst, with a slope value of 259 mV dec^{-1} (Fig. 6(c)). A lower Tafel slope value tells us about the faster kinetics of ions/charges throughout the HER mechanism, indicating an outstanding electrocatalytic performance of the prepared MOF.

The Tafel values provide insight into the HER mechanism, suggesting that it may proceed through the discharge-ion/discharge-combination mechanism.[54] In alkaline media, HER phases are represented by following equations.[55]

$H_2O + e^- \rightarrow H_{ads} + OH^-$ (120 mV dec^{-1}) Volmer reaction (discharge step)

$H_{ads} + H_{ads} \rightarrow H_2$ (30 mV dec^{-1}) Tafel reaction (combination step)

$H_{ads} + H_2O + e^- \rightarrow H_2 + OH^-$ (40 mV dec^{-1}) Heyrovsky reaction (ion step)

The HER response may correspond to the Volmer–Tafel mechanism if the Tafel value is 30 mV dec^{-1} or less, to the

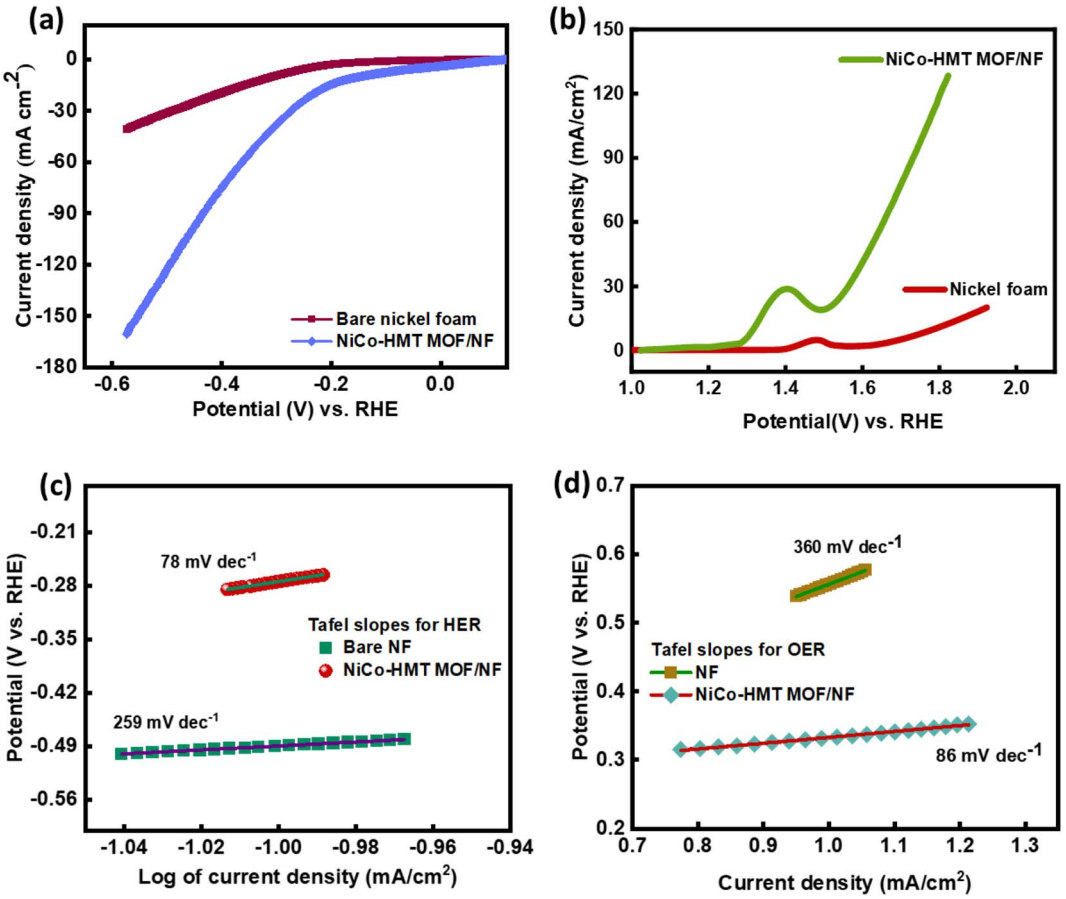

Fig. 6 (a) Polarization curves of bare NF and NiCo-MOF for hydrogen evolution reaction. (b) LSV profiles of required catalysts for oxygen evolution reaction. (c) Tafel plots for HER. (d) Tafel slopes for OER.

Volmer–Heyrovsky mechanism if the Tafel slope is 40 mV dec^{-1}, and to the Heyrovsky step if the slope value is above 40 mV dec^{-1}, along with rate-determining steps.[56] As both of the Tafel slopes obtained are above 40 mV dec^{-1}, this suggests that the H_2 evolution pathway can involve either the Tafel mechanism or Heyrovsky mechanism. The as-prepared sample NiCo-HMT MOF indicates remarkable electrocatalytic performance towards the hydrogen evolution mechanism. The main reason behind the distinct behavior of the NiCo-HMT, compared with other materials, is the organic linker (hexamethyl tetra-amine). MOFs consisting of distinct linking groups exhibit different electrocatalytic properties, as shown in Table 1. The presence of nitrogen atoms in the HMT linker can accelerate the reaction kinetics, leading to efficient H_2 evolution. The amine groups can serve as proton acceptors and donors, actively engaging in the proton reduction reaction. This active participation enhances the overall electrocatalytic efficiency of the NiCo-MOF.

Table 1 HER and OER performances of different electrocatalysts

Catalyst	Overpotential (mV)	Tafel slope (mV dec^{-1})	Current density (mA cm^{-2})	Substrate	Reference
2D NiCo-MOF	270 (OER)	35.4	50	Ni foam	63
Bulk NiCo-MOF	370 (OER)	57	50	NF	63
2D Ni-MOF@Fe-MOF	275 (OER)	54	10	GCE	64
$Ni_2P/MoO_2@MoS_2$	280 (OER)	85	10	Ti-foil	65
$Ni_2P/MoO_2@MoS_2$	159 (HER)	77	10	Ti-foil	65
NiCo-MOF/rGOAS	210 (HER)	61	10	Ni-mesh	66
Pt/C (acidic)	28 (HER)	33	10	—	67
Pt/C (alkaline)	43 (HER)	113	10	—	67
RuO_2	70 (OER)	61	10	—	68
NiCo-HMT MOF/NF	274 (HER)	78	30	NF	This work
	330 (OER)	86		NF	

Besides H_2 evolution, both the samples (bare NF and NiCo-MOF) were investigated for O_2 evolution at a scanning voltage of 5 mV s^{-1} in an alkaline electrolyte. The response of the electrodes towards the OER can be seen in Fig. 6(b). The small overpotential and onset potential values represent the exceptional behavior of the electrocatalyst towards the OER. The oxidation peak at around 1.42 V in the LSV profile of the NiCo-HMT MOF/NF corresponds to the oxidation of Ni^{2+} to $Ni^{3+/4+}$.[58] As oxygen evolution starts at a higher current density of 30 mA cm^{-2}, the overpotential was calculated to achieve the required current density. As illustrated in Fig. 6(b), η_{30} for the NiCo-MOF was 0.33 V, hinting at the excellent catalytic behavior of this MOF. Moreover, the NiCo-HMT MOF showed an overpotential value of 0.39 V at a j (current density) of 50 mA cm^{-2}, while the Ni foam demonstrated very poor current response and did not exceed a current density of 25 mA cm^{-2}. As for the bare NF, the reaction starts at a small current density, so it required an overpotential of 560 mV to reach η_{10}. These outcomes show that the NiCo-HMT MOF/NF electrocatalyst displays a small overpotential and elevated reaction kinetics. The results confirm that the synergistic influence of the dual metal ions (nickel and cobalt) can significantly decrease the overpotential required for oxygen evolution. Moreover, the Tafel slopes for each active material were evaluated from their linear sweep voltammograms (Fig. 6(d)). The Tafel slope for the bimetallic NiCo-MOF was 86 mV dec^{-1}, which is less than for Ni foam (360 mV dec^{-1}) calculated for η_{10}, suggesting efficient reaction kinetics. Thus, the prepared bimetallic MOF shows that faster OER kinetics can be influenced by the composition, number of active sites, surface structure, and electrocatalyst loading.

For the HER and OER analysis, the NiCo-HMT required a very low overpotential to reach a higher current density compared to the bare nickel foam substrate. This is due to the following characteristics of the prepared bimetallic NiCo-HMT-based electrocatalyst: (1) abundant active sites due to dual metals; (2) faster electron/charge transfer rate; (3) porosity and larger surface area; (4) synergistic effect of different metals in prepared bifunctional catalyst; and (5) durability rate. Thus, material optimization on the nickel foam maximizes the electrocatalytic performance of the as-prepared NiCo-HMT.

3.2.2 Impedance, cyclic voltammograms, and double-layer capacitance analysis. To gain insight into the conductive and interfacial properties of the synthesized electrodes, EIS measurements were conducted in the frequency range 0.1 Hz–100 kHz. The results of the EIS spectrum for the NiCo-MOF can be interpreted using the equivalent circuit and Nyquist plot shown in Fig. 7(a and b). The EIS technique is regularly used to analyze the interaction between electrode material and electrolyte ions. It offers information about the electrical properties of the electrode–electrolyte interface, including ion-transfer kinetics, resistance at the interface, and double-layer capacitance. The EIS plot for the NiCo-HMT MOF exhibits a very small semicircle at a high-frequency region, which indicates its superior conductivity. The point of overlap on the x-scale in the high-frequency domain of the EIS spectrum indicates the equivalent series resistance (ESR) of the sample, which holds information about the resistance between the electrolyte and electrode. Thus, the ESR calculated for the prepared sample is 1.7 Ω. This smaller value of the ESR for the NiCo-MOF makes it a highly suitable bimetallic material, exhibiting faster kinetics and higher conductivity. Furthermore, the existence of an angled line in the minimum frequency range is an indication of Warburg impedance, which arises due to either ion transport or diffusion kinetics in the electrolyte.[59] Warburg impedance can be employed to investigate the influence of porosity, surface roughness, and other structural components on the electrochemical performance of electrodes. The promising results for the NiCo-HMT MOF make it a viable and attractive material for numerous energy storage and conversion applications.

To estimate the ECSA, measurement of the double-layer capacitance is required. CV measurements for the NiCo-MOF at sweep speeds of 20, 40, 60, 80 100, and 120 mV s^{-1} within the potential range −0.5 V to −0.7 V (a non-faradaic window) *vs.* reversible H-electrode were performed to analyze C_{dl} for the HER, as presented in Fig. 7(c). In addition, the positive potential limit of 0.1–0.3 V was selected to measure the C_{dl} of the OER mechanism, as shown in Fig. 7(d).

Fig. 7(e and f) shows that the NiCo-MOF displays a C_{dl} value of 4 mF cm^{-2} for hydrogen evolution and 23 mF cm^{-2} for oxygen evolution, respectively, which also indicates the superior electrocatalytic behavior of the bimetallic NiCo-MOF for hydrogen production. C_{dl} data were derived from cyclic voltammetry profiles to assess the ECSA. Thus, the ECSA for the prepared samples was achieved by using the formula below.

$$\mathrm{ECSA} = \frac{C_{dl}}{C_s}$$

Here, C_s represents the specific capacitance at the electrode surface, estimated to be 0.04 mF cm^{-2} in an alkaline electrolyte.[60] Hence, the ECSA value was 575 cm^2 and 100 cm^2 for the oxygen and hydrogen evolution of the NiCo-MOF, respectively. The higher ECSA value indicates the better HER/OER performance of the electrocatalyst, by facilitating charge kinetics, additional active sites, optimizing material deposition and offering synergistic effects. In numerous electrochemical mechanisms, such as electrocatalysis, reactions occur at specific parts on the electrode surface. A larger surface area presents a greater number of sites for reactant molecules to interact with, thus elevating the overall reaction rate. The increased ECSA of the material could be attributed to the existence of carbon, which appears to function as an active site. However, it is important to note that not every carbon active site is effective for H_2 and O_2 evolution reactions. This observation reinforces the notion that metals are indeed true active sites for the HER and OER.[61,62]

3.2.3 Stability and durability analysis. Long-term durability is a significant feature for analyzing the electrocatalytic performance of active electrodes towards hydrogen and oxygen evolution over an extended time period in an alkaline medium. Herein, the stability of the NiCo-HMT MOF/NF-based electrocatalyst was assessed by conducting chronoamperometry (i–t) for a duration of 20 hours, maintaining a potential of −0.376 V. The chronoamperometry technique is used to measure the kinetics of the HER/OER by maintaining a constant current density of 10 mA cm^{-2} and measuring the resulting voltage with

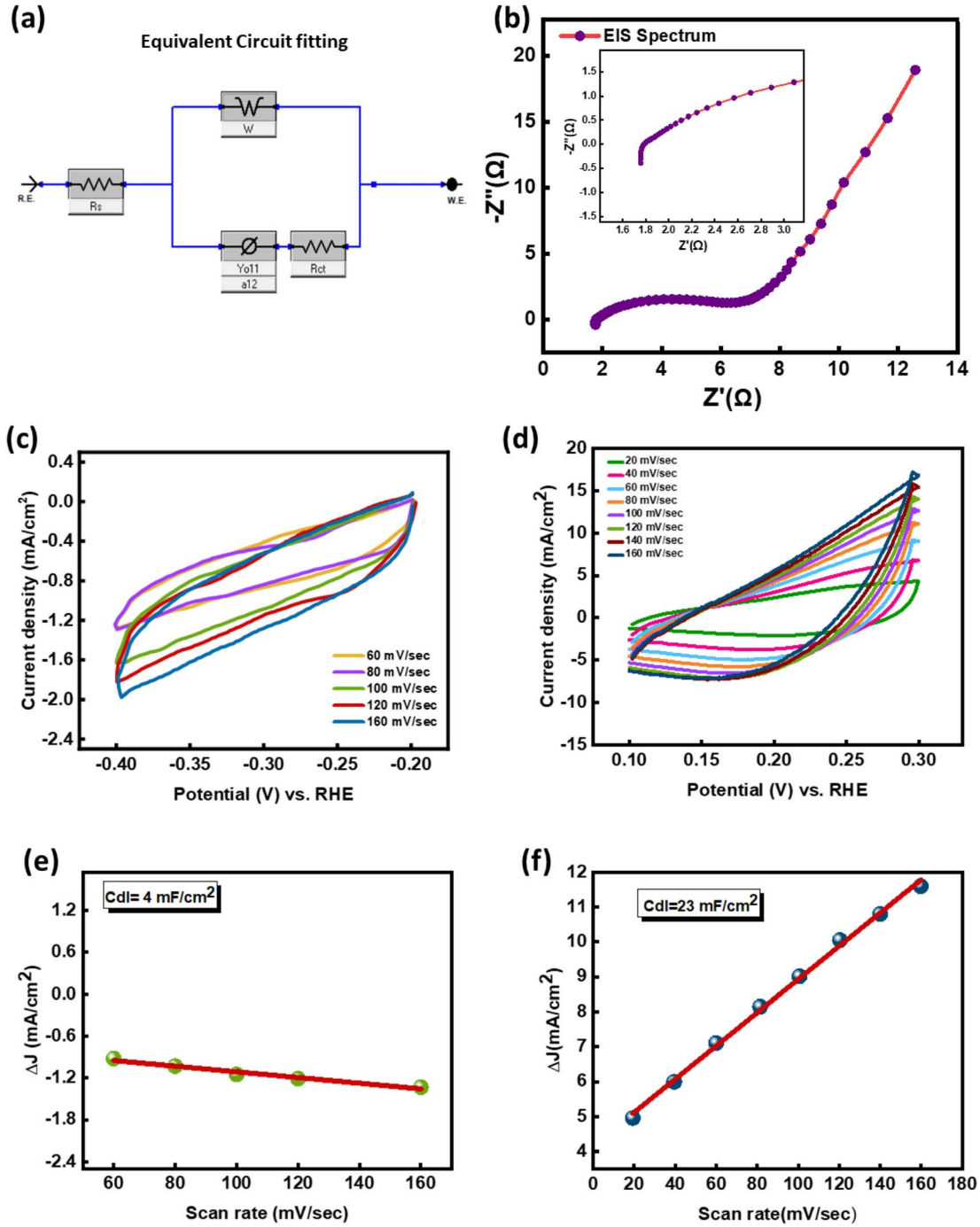

Fig. 7 (a) Equivalent circuit diagram. (b) Nyquist plot of NiCo-MOF with zoomed-in image in the inset. (c) Cyclic voltammograms of NiCo-MOF for HER. (d) CV scans for OER. (e) C_{dl} value of required sample in case of hydrogen evolution. (f) C_{dl} graph of oxygen evolution of the catalyst.

time, to evaluate the durability of the catalyst (NiCo-MOF). Fig. 8(b and d) shows LSV curves for the HER and OER analysis before and after the stability test. Polarization curves indicate a minor shift towards the higher overpotential region after the stability test. The main reasons behind this shift are as follows. (1) The primary curve shows the catalytic behavior of the required material, while, after the durability test, we analyze how well NiCo-HMT withstands prolonged electrocatalytic operation. (2) We analyzed the higher overpotentials of 307 mV and 350 mV for the HER and OER mechanisms by performing LSV tests after the stability operation because of the degradation of the material during continuous cycling for 20 h. (3) The small increase in overpotential values to reach the same current density after the stability test demonstrated the remarkable electrocatalytic characteristics and robustness of the prepared sample. Fig. 8(a and c) shows chronoamperometric results for the bifunctional catalyst after 20 hours. The profile indicates that the current density of this sample decreases to only 95% of

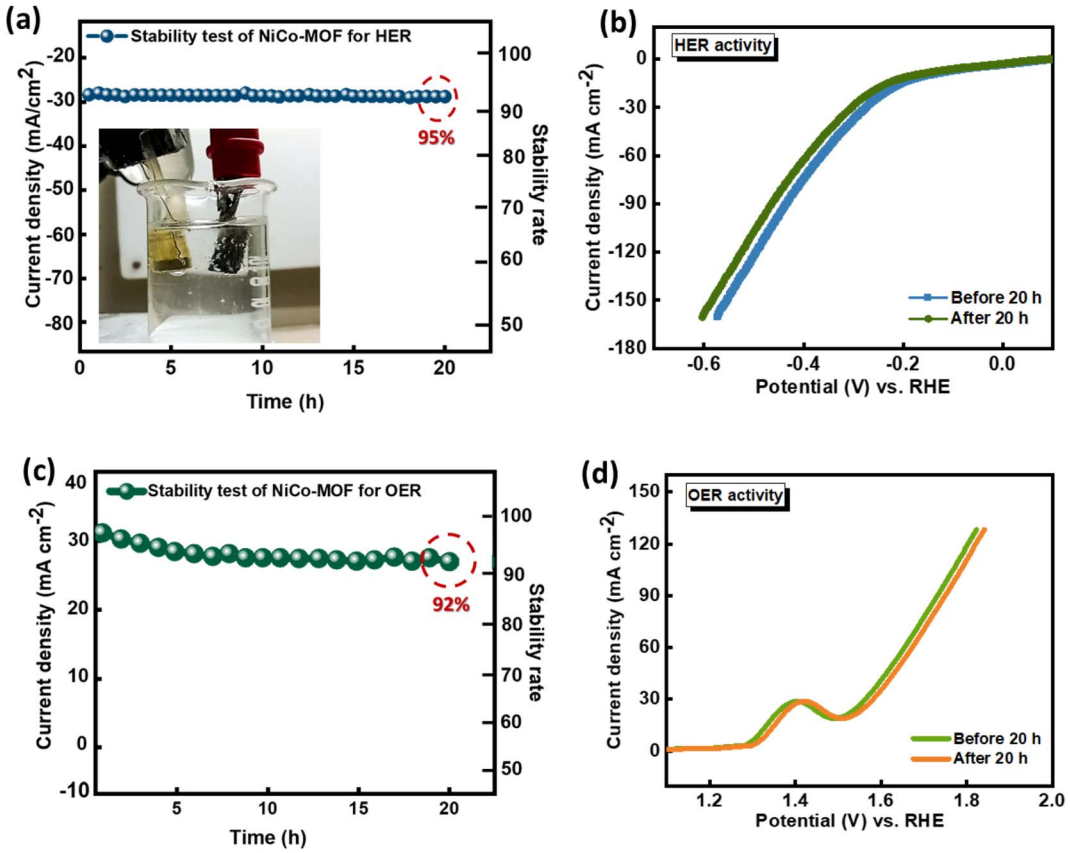

Fig. 8 (a) Stability test for HER of NiCo-MOF for continuous 20 h, along with its behavior after 20 h (see inset). (b) LSV curve for the prepared sample before and after stability test. (c) Stability test for OER mechanism for continuous 20 h testing. (d) LSV curves before and after CA analysis.

its primary value after 20 hours in H_2 evolution. The LSV analysis was carried out just after the chronoamperometry test, which shows that the hydrogen evolved at an overpotential of 307 mV. In addition, 92% retention of current density for the OER after continuous operation for 20 h was achieved, with a slight increase in overpotential value (350 mV) before CA analysis. Thus, it is clear from the LSV curves obtained, with minimal shifts, that the hexamethyl tetra-amine-based bimetallic nickel–cobalt MOF is a more stable electrocatalyst for energy conversion applications.

4. Conclusions

In conclusion, this investigation has demonstrated the first example of a hexamethyl tetra-amine-based nickel–cobalt MOF developed *via* a hydrothermal approach for efficient electrocatalytic OER and HER. The surface and bulk characteristics of the electrocatalyst, determined by utilizing techniques such as electron microscopy, X-ray methods, Raman spectroscopy, FTIR spectroscopy, and EDX, validate the preservation of the structural integrity and successful integration of individual components. Under alkaline conditions, the NiCo-HMT-based bifunctional electrocatalyst exhibited remarkable stability and significantly improved overall efficiency for H_2O splitting. The exceptional electrocatalytic efficiency can be attributed to several contributing factors, including: (1) the three-dimensional NiCo-MOF substrate, interlinked by HMT, not only enhances conductivity and structural stability but also facilitates rapid charge transfer, and it promotes the release of H_2 and O_2 bubbles at overpotentials of 274 mV and 330 mV, respectively; (2) its morphological characteristics result in abundant accessible active sites, a higher specific surface area, and enhanced charge/mass kinetics; and (3) its remarkable C_{dl} values of 23 mF cm^{-2} for oxygen evolution and 4 mF cm^{-2} for hydrogen evolution also indicate superior bifunctional electrocatalytic behavior towards water decomposition. The durability tests performed for continuous 20 h operation also prove the remarkable performance of the HMT-based NiCo-MOF. This study has revealed the first example of a hexamethyl tetra-amine-based nickel–cobalt MOF for both the HER and OER at high current density, making it a promising candidate for the commercialization of bimetallic electrocatalysts in alkaline medium for energy conversion applications.

Data availability

The data that support the findings of this study are confidential.

Author contributions

Rida Zahid: conceptualization, formal analysis, writing – original draft, methodology, data curation. Muhammad Ramzan

Abdul Karim: writing – review & editing, supervision, funding acquisition. Fahd Sikandar Khan: writing – review, investigation. Mohammad Mohsin Ali Marwat: visualization, writing – review & editing.

Conflicts of interest

The authors declare that they have no known competing financial interests or personal relationships that could have appeared to influence the work reported in this paper.

Acknowledgements

Muhammad Ramzan Abdul Karim acknowledges the valuable academic and research support from Ghulam Ishaq Khan (GIK) Institute of Engineering Sciences and Technology (Graduate Assistantship#GES2216).

References

1 J. Chen, *et al.*, Defective graphene aerogel-supported Bi–CoP nanoparticles as a high-potential air cathode for rechargeable Zn–air batteries, *J. Mater. Chem. A*, 2019, **7**(39), 22507–22513.
2 M. Xie, *et al.*, An Fe(TCNQ)2 nanowire array on Fe foil: an efficient non-noble-metal catalyst for the oxygen evolution reaction in alkaline media, *Chem. Commun.*, 2018, **54**(18), 2300–2303.
3 B. Zhang and S. Hu, Turning Ni-based hydroxide into an efficient hydrogen evolution electrocatalyst by fluoride incorporation, *Electrochem. Commun.*, 2018, **86**, 108–112.
4 D. Vikraman, *et al.*, Engineering the novel MoSe2-Mo2C hybrid nanoarray electrodes for energy storage and water splitting applications, *Appl. Catal., B*, 2020, **264**, 118531.
5 X. Liu, *et al.*, Noble metal–metal oxide nanohybrids with tailored nanostructures for efficient solar energy conversion, photocatalysis and environmental remediation, *Energy Environ. Sci.*, 2017, **10**(2), 402–434.
6 M. Sun, *et al.*, Earth-Rich Transition Metal Phosphide for Energy Conversion and Storage, *Adv. Energy Mater.*, 2016, **6**(13), 1600087.
7 G. T. M. Kadja, *et al.*, Recent advances of carbon nanotubes as electrocatalyst for in-situ hydrogen production and CO2 conversion to fuels, *Results Chem.*, 2023, **6**, 101037.
8 S. Hussain, *et al.*, One-Pot Synthesis of W(2)C/WS(2) Hybrid Nanostructures for Improved Hydrogen Evolution Reactions and Supercapacitors, *Nanomaterials*, 2020, **10**(8), 1597.
9 Y. Li, *et al.*, Ternary NiCoP nanosheet arrays: An excellent bifunctional catalyst for alkaline overall water splitting, *Nano Res.*, 2016, **9**(8), 2251–2259.
10 X. Gao, *et al.*, Synergizing in-grown Ni3N/Ni heterostructured core and ultrathin Ni3N surface shell enables self-adaptive surface reconfiguration and efficient oxygen evolution reaction, *Nano Energy*, 2020, **78**, 105355.
11 G. A. Ferrero, *et al.*, Fe–N-Doped Carbon Capsules with Outstanding Electrochemical Performance and Stability for the Oxygen Reduction Reaction in Both Acid and Alkaline Conditions, *ACS Nano*, 2016, **10**(6), 5922–5932.
12 T. Shaker, H. Mehdipour and A. Z. Moshfegh, Low loaded MoS2/Carbon cloth as a highly efficient electrocatalyst for hydrogen evolution reaction, *Int. J. Hydrogen Energy*, 2022, **47**(3), 1579–1588.
13 M. Zubair, *et al.*, 2D MXenes and their heterostructures for HER, OER and overall water splitting: a review, *Int. J. Hydrogen Energy*, 2022, **47**(5), 2794–2818.
14 W. Li, *et al.*, Hydrothermal Synthesis of Monolithic Co3Se4 Nanowire Electrodes for Oxygen Evolution and Overall Water Splitting with High Efficiency and Extraordinary Catalytic Stability, *Adv. Energy Mater.*, 2017, **7**(17), 1602579.
15 H. Li, *et al.*, Cobalt Phosphide Composite Encapsulated within N,P-Doped Carbon Nanotubes for Synergistic Oxygen Evolution, *Small*, 2018, **14**(19), e1800367.
16 X. Du, *et al.*, Monodisperse and self-assembled Pt-Cu nanoparticles as an efficient electrocatalyst for the methanol oxidation reaction, *J. Mater. Chem. A*, 2016, **4**(5), 1579–1585.
17 G.-f. Long, *et al.*, Pt/CN-doped electrocatalysts: Superior electrocatalytic activity for methanol oxidation reaction and mechanistic insight into interfacial enhancement, *Appl. Catal., B*, 2017, **203**, 541–548.
18 Q. Lu, *et al.*, 2D Transition-Metal-Dichalcogenide-Nanosheet-Based Composites for Photocatalytic and Electrocatalytic Hydrogen Evolution Reactions, *Adv. Mater.*, 2016, **28**(10), 1917–1933.
19 M. Li, *et al.*, A novel flower-like architecture of FeCo@NC-functionalized ultra-thin carbon nanosheets as a highly efficient 3D bifunctional electrocatalyst for full water splitting, *J. Mater. Chem. A*, 2017, **5**(11), 5413–5425.
20 D.-Y. Kang and J. S. Lee, Challenges in Developing MOF-Based Membranes for Gas Separation, *Langmuir*, 2023, **39**(8), 2871–2880.
21 J. Rajendran, Amperometric determination of salivary thiocyanate using electrochemically fabricated poly (3, 4-ethylenedioxythiophene)/MXene hybrid film, *J. Hazard. Mater.*, 2023, **449**, 130979.
22 C. Yan, *et al.*, 2D Nanomaterial Supported Single-Metal Atoms for Heterogeneous Photo/Electrocatalysis, *Adv. Funct. Mater.*, 2023, **33**(5), 2210837.
23 W. Zhou, *et al.*, MOF derived metal oxide composites and their applications in energy storage, *Coord. Chem. Rev.*, 2023, **477**, 214949.
24 Y. Lü, *et al.*, MOF-Templated Synthesis of Porous Co3O4 Concave Nanocubes with High Specific Surface Area and Their Gas Sensing Properties, *ACS Appl. Mater. Interfaces*, 2014, **6**(6), 4186–4195.
25 D. Sheberla, *et al.*, Conductive MOF electrodes for stable supercapacitors with high areal capacitance, *Nat. Mater.*, 2017, **16**(2), 220–224.
26 A. Banerjee, *et al.*, Superior lithium storage properties of α-Fe2O3 nano-assembled spindles, *Nano Energy*, 2013, **2**(5), 890–896.

27 L. Mei, W.-Q. Shi and Z.-F. Chai, Ordered Entanglement in Actinide-Organic Coordination Polymers, *Bull. Chem. Soc. Jpn.*, 2018, **91**(4), 554–562.
28 J.-S. Li, *et al.*, Polydopamine-assisted construction of cobalt phosphide encapsulated in N-doped carbon porous polyhedrons for enhanced overall water splitting, *Carbon*, 2019, **145**, 694–700.
29 M. Zhang, *et al.*, Novel MOF-Derived Co@N-C Bifunctional Catalysts for Highly Efficient Zn–Air Batteries and Water Splitting, *Adv. Mater.*, 2018, **30**(10), 1705431.
30 P. He, X.-Y. Yu and X. W. Lou, Carbon-Incorporated Nickel–Cobalt Mixed Metal Phosphide Nanoboxes with Enhanced Electrocatalytic Activity for Oxygen Evolution, *Angew. Chem., Int. Ed.*, 2017, **56**(14), 3897–3900.
31 X. Yu, *et al.*, Nitrogen and Sulfur Codoped Graphite Foam as a Self-Supported Metal-Free Electrocatalytic Electrode for Water Oxidation, *Adv. Energy Mater.*, 2016, **6**(2), 1501492.
32 K. Lemoine, *et al.*, Amorphous Iron–Manganese Oxyfluorides, Promising Catalysts for Oxygen Evolution Reaction under Acidic Media, *ACS Appl. Energy Mater.*, 2021, **4**(2), 1173–1181.
33 Z. Liu, *et al.*, Strategies to improve electrochemical performances of pristine metal-organic frameworks-based electrodes for lithium/sodium-ion batteries, *SmartMat*, 2021, **2**(4), 488–518.
34 L. Yaqoob, *et al.*, Electrochemical synergies of Fe–Ni bimetallic MOF CNTs catalyst for OER in water splitting, *J. Alloys Compd.*, 2021, **850**, 156583.
35 B. Iqbal, *et al.*, One-Pot Synthesis of Heterobimetallic Metal–Organic Frameworks (MOFs) for Multifunctional Catalysis, *Chem.–Eur. J.*, 2019, **25**(44), 10490–10498.
36 B. Song, *et al.*, Tuning Mixed Nickel Iron Phosphosulfide Nanosheet Electrocatalysts for Enhanced Hydrogen and Oxygen Evolution, *ACS Catal.*, 2017, **7**(12), 8549–8557.
37 Z. Xue, *et al.*, Revealing Ni-based layered double hydroxides as high-efficiency electrocatalysts for the oxygen evolution reaction: a DFT study, *J. Mater. Chem. A*, 2019, **7**(40), 23091–23097.
38 K.-L. Yan, *et al.*, Organic-inorganic hybrids-directed ternary NiFeMoS anemone-like nanorods with scaly surface supported on nickel foam for efficient overall water splitting, *Chem. Eng. J.*, 2018, **334**, 922–931.
39 C. Ray, *et al.*, Stacked Porous Iron-Doped Nickel Cobalt Phosphide Nanoparticle: An Efficient and Stable Water Splitting Electrocatalyst, *ACS Sustain. Chem. Eng.*, 2018, **6**(5), 6146–6156.
40 B. Cui, *et al.*, Efficient multifunctional electrocatalyst based on 2D semiconductive bimetallic metal-organic framework toward non-Pt methanol oxidation and overall water splitting, *J. Colloid Interface Sci.*, 2020, **578**, 10–23.
41 C. Yang, *et al.*, Performance enhancement of oxygen evolution reaction through incorporating bimetallic electrocatalysts in two-dimensional metal–organic frameworks, *Catal. Sci. Technol.*, 2020, **10**(12), 3897–3903.
42 F. Zuhri, *et al.*, ZnO-FC-NiCo MOF for prospective supercapacitor materials, *Mater. Today: Proc.*, 2021, **44**, 3385–3389.
43 N. Jabeen, *et al.*, Unique Core–Shell Nanorod Arrays with Polyaniline Deposited into Mesoporous NiCo2O4 Support for High-Performance Supercapacitor Electrodes, *ACS Appl. Mater. Interfaces*, 2016, **8**(9), 6093–6100.
44 A. Abbasi, *et al.*, New interpenetrated mixed (Co/Ni) metal–organic framework for dye removal under mild conditions, *Inorg. Chim. Acta*, 2016, **439**, 18–23.
45 T. Ungár, Microstructural parameters from X-ray diffraction peak broadening, *Scr. Mater.*, 2004, **51**(8), 777–781.
46 M. Fan, D. Dai and B. Huang, Fourier transform infrared spectroscopy for natural fibres, *Fourier Transform: Mater. Anal.*, 2012, **3**, 45–68.
47 Y.-M. Zhang, Q.-Y. Xu and Y. Liu, Molecular recognition and biological application of modified β-cyclodextrins, *Sci. China: Chem.*, 2019, **62**, 549–560.
48 T. Wang, *et al.*, 2-Methylimidazole-Derived Ni–Co Layered Double Hydroxide Nanosheets as High Rate Capability and High Energy Density Storage Material in Hybrid Supercapacitors, *ACS Appl. Mater. Interfaces*, 2017, **9**(18), 15510–15524.
49 A. El Oudiani, S. Msahli and F. Sakli, In-depth study of agave fiber structure using Fourier transform infrared spectroscopy, *Carbohydr. Polym.*, 2017, **164**, 242–248.
50 D. Voiry, *et al.*, Enhanced catalytic activity in strained chemically exfoliated WS2 nanosheets for hydrogen evolution, *Nat. Mater.*, 2013, **12**(9), 850–855.
51 Z. Liu, *et al.*, Colloidal synthesis of 1T' phase dominated WS2 towards endurable electrocatalysis, *Nano Energy*, 2018, **50**, 176–181.
52 X. Yuan, *et al.*, One-pot self-assembly and photoreduction synthesis of silver nanoparticle-decorated reduced graphene oxide/MIL-125(Ti) photocatalyst with improved visible light photocatalytic activity, *Appl. Organomet. Chem.*, 2016, **30**(5), 289–296.
53 G. Yan, *et al.*, N-Carbon coated P-W2C composite as efficient electrocatalyst for hydrogen evolution reactions over the whole pH range, *J. Mater. Chem. A*, 2017, **5**(2), 765–772.
54 S. Kumaraguru, J. Yesuraj and S. Mohan, Reduced graphene oxide-wrapped micro-rod like Ni/Co organic-inorganic hybrid nanocomposite as an electrode material for high-performance supercapacitor, *Composites, Part B*, 2020, **185**, 107767.
55 Y. Han, *et al.*, Direct carbonization of cobalt-doped NH2-MIL-53(Fe) for electrocatalysis of oxygen evolution reaction, *Nanoscale*, 2016, **8**(2), 1033–1039.
56 C. Cheng, *et al.*, In Situ Growth of Nickel–Cobalt Metal Organic Frameworks Guided by a Nickel–Molybdenum Layered Double Hydroxide with Two-Dimensional Nanosheets Forming Flower-Like Struc-Tures for High-Performance Supercapacitors, *Nanomaterials*, 2023, **13**(3), 581.
57 M. R. Abdul Karim, *et al.*, Solvothermal Synthesis of Flower-Flakes Like Nano Composites of Ni-Co Metal Organic Frameworks and Graphene Nanoplatelets for Energy Storage Applications, *ECS J. Solid State Sci. Technol.*, 2022, **11**(1), 011001.

58 H. Trzesniowski, *et al.*, Reversible and Irreversible Cation Intercalation in NiFeOx Oxygen Evolution Catalysts in Alkaline Media, *J. Phys. Chem. Lett.*, 2023, **14**(2), 545–551.
59 F. S. Omar, *et al.*, Binary composite of polyaniline/copper cobaltite for high performance asymmetric supercapacitor application, *Electrochim. Acta*, 2017, **227**, 41–48.
60 W. Yaseen, *et al.*, Cobalt–Iron nanoparticles encapsulated in mesoporous carbon nanosheets: A one-pot synthesis of highly stable electrocatalysts for overall water splitting, *Int. J. Hydrogen Energy*, 2021, **46**(7), 5234–5249.
61 N. Ullah, *et al.*, In situ growth of M-MO (M = Ni, Co) in 3D graphene as a competent bifunctional electrocatalyst for OER and HER, *Electrochim. Acta*, 2019, **298**, 163–171.
62 L. Wang, *et al.*, Ni nanoparticles supported on graphene layers: An excellent 3D electrode for hydrogen evolution reaction in alkaline solution, *J. Power Sources*, 2017, **347**, 220–228.
63 P. Thangasamy, S. Shanmuganathan and V. Subramanian, A NiCo-MOF nanosheet array based electrocatalyst for the oxygen evolution reaction, *Nanoscale Adv.*, 2020, **2**(5), 2073–2079.
64 X.-g. Peng, *et al.*, Preparation and investigation of Fe-MIL-101 as efficient catalysts for oxygen evolution reaction, *J. Fuel Chem. Technol.*, 2021, **49**(9), 1354–1361.
65 Y. Wang, *et al.*, Unique hybrid Ni2P/MoO2@MoS2 nanomaterials as bifunctional non-noble-metal electrocatalysts for water splitting, *Nanoscale*, 2017, **9**(44), 17349–17356.
66 M. Khalid, *et al.*, Nano-flocks of a bimetallic organic framework for efficient hydrogen evolution electrocatalysis, *Chem. Commun.*, 2018, **54**(78), 11048–11051.
67 Y. Liu, *et al.*, Hierarchical Porous Molybdenum Carbide Based Nanomaterials for Electrocatalytic Hydrogen Production, *Front. Chem.*, 2020, **8**, 426.
68 Y. Lee, *et al.*, Synthesis and Activities of Rutile IrO2 and RuO2 Nanoparticles for Oxygen Evolution in Acid and Alkaline Solutions, *J. Phys. Chem. Lett.*, 2012, **3**(3), 399–404.